Biosensors and Bioelectronics 129 (2019) 208–215

Contents lists available at ScienceDirect

Biosensors and Bioelectronics

journal homepage: www.elsevier.com/locate/bios

FEM-based design of optical transparent indium tin oxide multielectrode arrays for multiparametric, high sensitive cell based assays

Heinz-Georg Jahnke[1], Sabine Schmidt[1], Ronny Frank, Winnie Weigel, Christoph Prönnecke, Andrea A. Robitzki*

Centre for Biotechnology and Biomedicine, Molecular Biological-biochemical Processing Technology, Leipzig University, Deutscher Platz 5, D-04103 Leipzig, Germany

ARTICLE INFO

Keywords:
Optical transparent indium tin oxide electrodes
Multielectrode array optimization
Cell-electrode equivalent circuit model
FEM simulated indium tin oxide electrodes

ABSTRACT

Multielectrode array (MEA) technology is widely used for the bioelectronic monitoring of cellular alterations. In general, noble metal based MEAs are preferred e.g. for impedance spectroscopy because of their high conductivity and biocompatibility. Today's research focuses on combining different readout methods in a single measurement setup, such as sensitive electronic and optical readouts, where noble metal-based electrodes are excluded and transparent electrodes and optimized MEAs are required. In this context, we used optical transparent indium tin oxide (ITO) as electrode material. As a drawback, the decreased conductivity can lead to drastically decreased cell signals and it is hardly to predict which layout changes lead to a substantial signal increase. To overcome this limitation, we introduce an approach where equivalent circuit modelling (ECM) on reference multielectrode arrays is used to determine cell type specific electrical parameters, which then are used in finite element method (FEM) simulations to predict achievable cell signals and signal-noise-ratios (SNR) and thus use simulation to efficiently optimize multielectrode arrays.

To evaluate our approach, MEAs with a wide range of electrode sizes were fabricated with ITO and gold. HEK-A cells were used to compare achievable cell signals for impedimetric monitoring. Our study revealed that especially for large ITO electrodes, the sensitivity drastically decreases. To overcome this drawback, we designed an optimized dual layer ITO MEA with gold support structures and more strikingly, successfully predict the cell signal increase by using our combined ECM and FEM simulation based approach.

1. Introduction

Micro- and mesoelectrode structures for bioelectronic monitoring of cells and cellular alterations were established in 1970´s and 1980´s mainly using impedance spectroscopy (Giaever and Keese, 1984) as well as surface potential amplification for electrophysiological monitoring (Thomas et al., 1972). From the very beginning, gold or platinum were the preferred electrode material due to their high biocompatibility, stability in cell culture medium and moreover high conductivity. Since the missing optical transparency for microscopy was a drawback, the search for transparent electrode material was in focus. In this context, indium tin oxide (ITO) as a semiconductor material was identified early as an alternative (Gross et al., 1985) and remains the only widely used transparent optical electrode material for cell applications (Choi et al., 2007; Kisler et al., 2012) from which microelectrode arrays are also commercially available (Jahnke et al., 2009). With respect to its clear advantages such as the optical transparency and the much lower costs in comparison to gold and platinum, ITO multielectrode arrays are still minor used. In this context, it is remarkable that only microelectrodes are made of ITO (Jahnke et al., 2009; Kisler et al., 2012; Panke et al., 2011). Although large ITO electrodes were already used for electrochemical enzyme characterization (Frank et al., 2017, 2018), large electrodes for cell monitoring would benefit clearly from the optical transparency of ITO, but to date only are made of gold or platinum (Eichler et al., 2015; Solly et al., 2004; Thakur et al., 2012). Besides the much more complex processing with respect to optimum electrical and optical characteristic, the overall limitation of ITO is the conductivity that is 2–3 magnitude lower than for gold. Nevertheless, there are no detailed studies available that systematically analyze the quantitative relation between electrode size/geometry, electrode impedance and moreover conducting paths influence in a multielectrode array setup and most important influence on the achievable cell signal and signal-noise-ratio (SNR). Moreover, our aim was not only to analyze certain electrode configurations and MEA types for an empirical

* Corresponding author.
E-mail address: andrea.robitzki@bbz.uni-leipzig.de (A.A. Robitzki).
[1] These authors contributed equally to this work.

https://doi.org/10.1016/j.bios.2018.09.095
Received 30 June 2018; Received in revised form 4 September 2018; Accepted 27 September 2018
Available online 28 September 2018
0956-5663/

description but we also want to find an approach to simulate electrode and array structures including the achievable cell signals and therefore, offer the opportunity to design and rationally optimize multielectrode arrays in silico instead of trial and error real fabrication cycles. In this context, we focused on FEM simulation, which were suitable in the past for recapitulating complex electrode-electrolyte as well as electrode-cell interactions (Canali et al., 2015; Schmid et al., 2016; Zitzmann et al., 2017). Thus, we aimed to analyze reference electrode systems with a typical cell culture model and use the measurement data to validate FEM simulation derived data and findings.

2. Materials and methods

2.1. Fabrication of multielectrode arrays

Glass substrates were intensively cleaned and prepared with photoresist to form conducting paths and electrodes (see Supplementary information for details). Coating with conductive materials such as ITO and Au was fabricated by a sputtering process in a high vacuum device (CREAMET 500, CREAVAC GmbH) at 4×10^{-4} mbar working pressure with a working distance of 150 mm (between target and substrate). Details for ITO processing, the gold layer sputtering, SU-8 passivation layer and atomic force microscopic characterization see Supplementary information.

2.2. Electrochemical impedance spectroscopy

Impedance spectra were acquired using the high-precision impedance analyzer Agilent 4294A (Agilent Technologies) with 10 mV alternating voltage in a frequency range of 500 Hz to 1 MHz. in combination with a self-developed multiplexer frontend and controlling software (IMAT v.2.5.3). The self-developed software IDAT v3.6.5.2 was used to calculate the relative impedance ((|Z|covered − |Z|cell-free)/|Z|cell-free × 100%), which represents the cell signal. For impedimetric monitoring of cells, the self-developed multiplexer frontend was placed in a cell incubator with 37 °C and 5% CO_2 in a humidified atmosphere.

2.3. Equivalent circuit modelling

To obtain the electrical cellular parameters a simplified electronic equivalent circuit model of the cell-electrode-interface (see results section) was used to perform a fitting of measured impedance magnitude and phase angle spectra. The electrical cellular parameters were determined in a two-step optimization process. Therefore, we used a self-developed software based on the LabView development suite (National Instruments). In the first step, the electrode-electrolyte dependent parameters CPE_{el} (constant phase element) and R_S (spreading resistance) were obtained using an equivalent circuit without the cell parameters C_{Cell} (cellular capacitance) and R_{Cell} (cellular resistance). In the second step, the complete equivalent circuit was applied on impedance magnitude and phase angle spectra of cell-covered electrode whereas the parameters from the first step were kept constant. The spectra fitting was realized by a Levenberg-Marquardt based constrained optimization algorithm that is provided by the LabView build in toolbox.

2.4. Finite element method (FEM) simulation

FEM simulation was done using the AC/DC-module of COMSOL Multiphysics 5.3 (Comsol Multiphysics GmbH). Multielectrode array layouts were constructed in AutoCAD 2016 (Autodesk) needed culture medium properties, in detail relative permittivity (80) and electrical conductivity (1.5 S/m) were taken from the literature (Mittal et al., 2007; Zitzmann et al., 2017). For simulating the impedance measurement, an alternating electrical field with 10 mV amplitude at the measurement electrode and a ground connection at the counter electrode was applied. To assign the electrode-electrolyte double-layer, a contact impedance was applied between the electrode surface and the medium with capacitance values that were derived by the equivalent circuit model analysis. The simulation was done using a fully coupled direct solver with the mesh size fine.

2.5. Cell culture

For measurements on an eukaryotic cell culture model, HEK-A cells (Life Technologies) were used and cultured in a supplemented DMEM medium as previously described (Zitzmann et al., 2017). For details of the MEA coating and viability staining see Supplementary information. For obtaining a confluent layer 100,000 cells per well were seeded in 250 µl culture medium and cultured for 48 h in a cell culture incubator. For live imaging of the cell membrane a self-established HEK-A cell line, which was stably transfected with a construct leading to expression of a GFP with farnesylation tag was used.

2.6. Statistics

For statistical analyses, Graphpad Prism 5.02 was used. In general, the presented data graphs and charts shows mean values ± standard error of mean (sem). Comparison between two groups were analyzed using an unpaired *t*-test. Multiple group comparisons were done by ANOVA and Sidak post-hoc test.

3. Results and discussion

3.1. Indium tin oxide and gold electrodes differ in surface topology and electrochemical characteristics

For a detailed investigation of the characteristics of transparent indium tin oxide (ITO) multielectrode arrays for cell-based assays we have chosen two different array types (Fig. 1A), one with microelectrodes of three different diameters (50 µm, 100 µm, 200 µm) and another with large, symmetric interdigital electrodes with a geometric area of 5.15 mm^2 of each finger (Supplementary Fig. S1A, B). In contrast to the microelectrode array, this results in a culture surface coverage of 30% by the electrodes. Each array comprises of nine wells that fulfill the dimensions of 96 well ANSI format (Supplementary Fig. S1C). As a reference, all arrays were also produced using gold (Au) for conducting paths and electrodes. From our empirical derived experience, we produced the arrays with an electrode layer thickness of 700 nm that at least for gold definitively exclude conducting paths limitations for such small arrays. First, an atomic force microscopic (AFM) analysis was performed, since drastic differences in surface topology can clearly influence electrode-electrolyte characteristics (Frank et al., 2018) as well as cell adhesion behavior and therefore, have to be taken into account. The image analysis of three independently produced array sets (n = 3 experiments) revealed a clearly rougher surface for the ITO electrodes in comparison to gold electrodes (4.28 ± 0.09 nm vs. 1.67 ± 0.03 nm). However, the calculated real surface area showed only small surface area increase of 4.9 ± 0.6% for ITO in comparison to 1.0 ± 0.1% for Au. Although this increase is significant, this small effect of a 2.6 nm roughness increase is negligible in the context of cellular alterations like cell adhesion (Zareidoost et al., 2012), especially with regard to the cell adhesion promoting collagen I coating that levels out such small surface differences.

Based on this finding, we continued with the impedance spectroscopy based characterization of both array types and materials in combination with HEK-A cell culture medium as electrolyte (Fig. 1C). Since for impedimetric monitoring of cells and cellular alterations the β–dispersion (kHz range) is in focus (Dean et al., 2008), we recorded all spectra from 500 Hz to 1 MHz. The impedance spectra from three independent produced arrays (n = 3 experiments) were analyzed

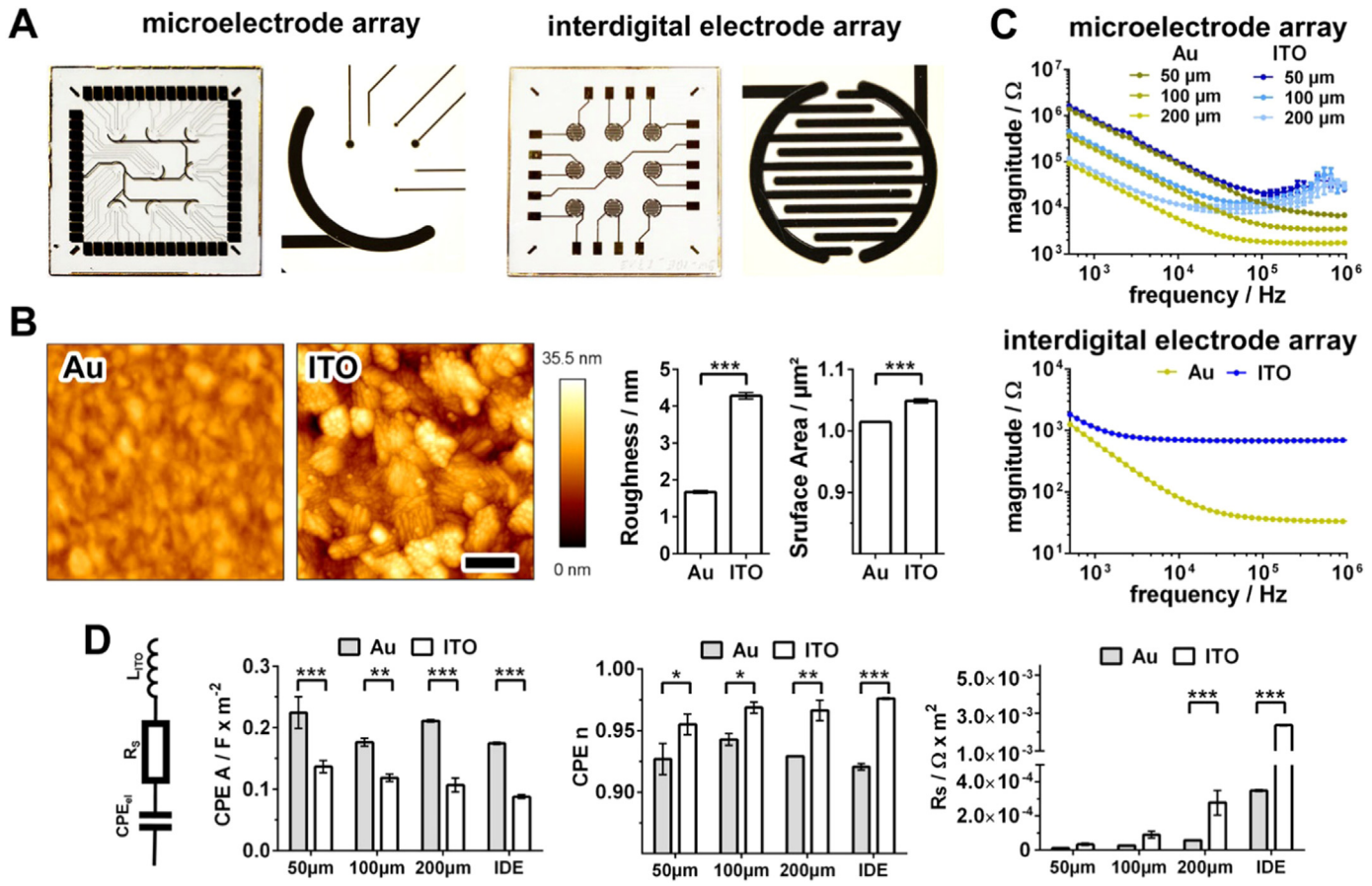

Fig. 1. Characterization of gold and indium tin oxide multielectrode arrays. (A) Two reference chip layouts with microelectrodes of 50 µm, 100 µm, and 200 µm diameter as well as large area interdigital electrodes. (B) Atomic force microscopy based surface topology analysis for Au and ITO electrodes (scale bar = 200 nm). The surface roughness (R_a) and the real surface area (per 1 µm^2) were derived from topology images (n = 3, mean ± sem, *** $p < 0.001$). Scheme of the measurement system. (C) Characteristic impedance magnitude spectra of both array types made of gold (Au) and indium tin oxide (ITO) (n = 3, mean ± sem). (D) Equivalent circuit model for impedance data fitting and statistical analysis of equivalent circuit model derived electrode parameters (CPE_A and CPE_n) as well as the spreading resistance (R_S) (n = 3, mean ± sem, * $p < 0.05$, ** $p < 0.01$, *** $p < 0.001$).

whereas all electrode spectra of one array (9 for IDE and 18 for each electrode size on the microelectrode array) were considered as replicates and averaged per array. As expected, the impedance magnitude clearly depends on the electrode size. Similarly, the linear proportion of the graphs in the lower frequency range increases with a decreasing electrode size. The comparison of the materials revealed a clearly higher impedance magnitude for ITO electrodes in the higher frequency range that increased with electrode size. Thus, for the smallest electrodes (50 µm diameter) the differences between Au und ITO electrodes were the smallest. Additionally, for the ITO microelectrodes an impedance magnitude increase was observed for frequencies above 100 kHz that means there has to be an inductive effect. This was not visible for the large size IDEs nor the Au electrodes. Although, we intensively searched the literature, we were not able to find an explanation for this ITO specific effect in the context of ITO microelectrodes in combination with isotonic electrolytes or cell culture medium. However, we had to consider the inductive effect in the following fitting of ITO microelectrode impedance spectra based on an equivalent circuit diagram (Fig. 1D). The electrode-electrolyte interface could be described by a constant phase element (CPE) in addition to the spreading resistance of the culture medium. The electrode size adjusted values revealed for CPE_A (CPE capacitance parameter) values in the range of 0.175–0.225 F/m^2 for gold electrodes. CPE_A values of ITO electrodes were always significantly lower with an increasing trend for smaller electrode size (0.088–0.137 F/m^2). For CPE_n (CPE exponent parameter) Au electrodes revealed values in the range of 0.92–0.94 with no observable trend with regard to electrode size. For ITO electrodes, values were always significant higher with an increasing trend for larger electrodes (0.96–0.98). Since a CPE_n of 1 represents an ideal capacitance, the observed values represents an almost ideal capacitance. Small deviations from 1 are in general attributed to adsorption of surface impurities (Martin and Lasia, 2011). The clearest differences were observed for the spreading resistances with a significant increase for larger electrodes, while ITO electrodes always had significantly higher values than Au electrodes. For the IDEs the value was nearly ten-fold higher (ITO 2.4×10^{-3} Ω × m^2, Au 3.5×10^{-4} Ω × m^2). At this point, it has to be mentioned that this resistance in series to the CPE not only reflects the electrolyte spreading resistance. While this should mainly be the case for the highly conductive material gold, for ITO the track resistance of the conducting paths contributes to the total resistance. However, this will be analyzed in detail at a later point.

3.2. Arrays with large size ITO electrodes show drastic cell signal loss

After the detailed array characterization that revealed distinct impedimetric characteristics with partially higher self-impedance values for the ITO electrodes, we focused on the question how this will influence the cell signals that can be achieved with the different electrode sizes and materials. Therefore, from each array type and material three independently fabricated arrays (n = 3 experiments) were taken and HEK-A cells cultivated on them for 48 h until a confluent cell layer was obtained. This was verified before the impedimetric analysis by

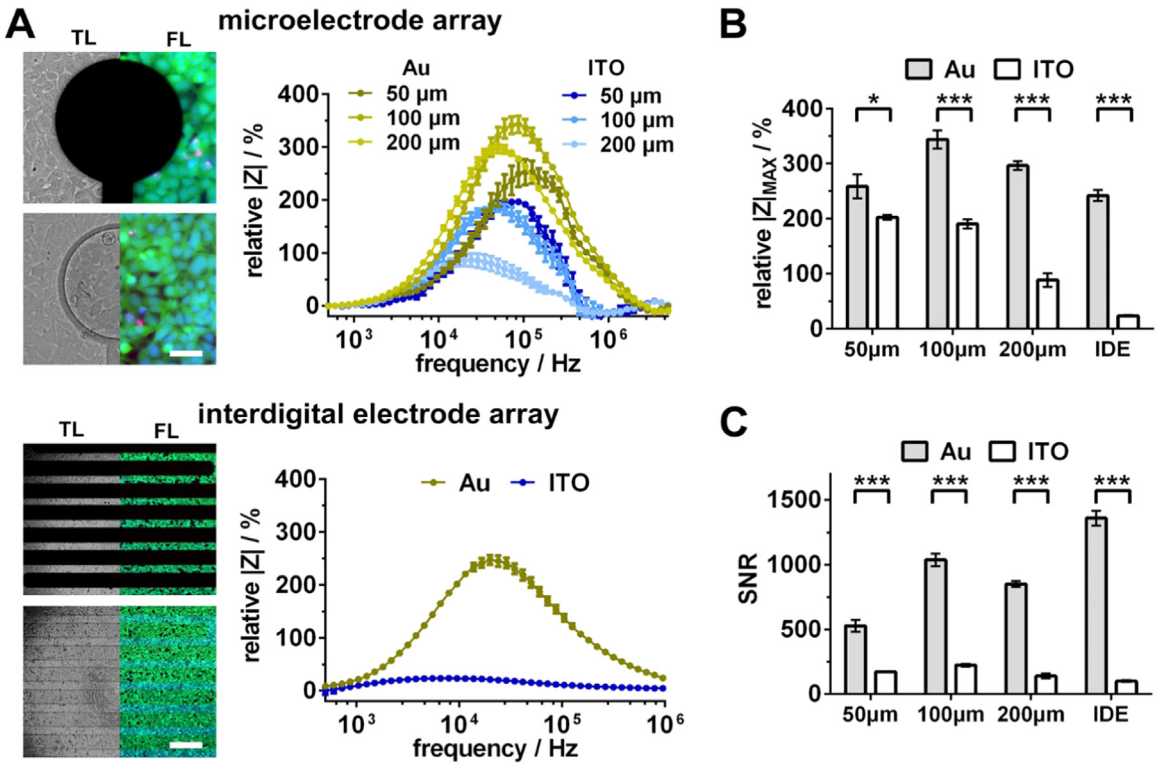

Fig. 2. Electrode size and material dependent cell signal analysis. (A) HEK-A cells were cultured on both array types made of Au and ITO for 48 h until a confluent cell layer was established. Confluence and vitality of the cell layer were detected by transmission light (TL) and fluorescence vitality stain (FL). In detail cell nuclei (blue), damaged cells (red) and metabolic active cytosol (green) was stained (scale bar = 50 µm for microelectrode array and 400 µm for IDE array). The cell signal (relative impedance) was extracted from the impedance magnitude spectra (n = 3, mean ± sem). (B) Statistical analysis of the maximum cell signal and (C) the signal-to-noise ratio (SNR) (n = 3, mean ± sem, *** $p < 0.001$).

transmission microscopy (Fig. 2A) as well as after the measurement by a vitality staining with different fluorophores. All images verified a vital and confluent cell layer. Moreover, it demonstrated the big advantage of ITO electrodes with regard to optical transparency. Thus, the direct observation of the cells on the electrode was perfectly possible.

From the recorded impedance magnitude spectra the relative impedance was calculated, which represents the cellular contribution to the impedance magnitude spectrum (cell signal). For the microelectrode arrays both materials revealed distinct signals of several hundred percent and similar spectra shapes with maximum values in the range of 20–100 kHz but lower maximum values for the ITO electrodes. In contrast, the large size electrode (IDE) arrays showed extreme differences in the signal height with an extremely low cell signal for the ITO arrays. The statistical analysis of the maximum cell signal verified this observation with significant lower maximum cell signals for ITO electrodes while the difference increases with increased electrode size. Thus, ITO electrodes show a loss of cell signal of 20% for 50 µm, 44% for 100 µm, 70% for 200 µm as well as drastic 91% for IDE electrodes. Additionally, the maximum signal decreases for each material with increased electrode size except the smallest electrode size (50 µm diameter). In general, the cell signal should increase with decreased electrode size since the mainly cell membrane caused impedance correlates inversely quadratically with the electrode size while the electrolyte influences the impedance only linearly (Fuller and Harb, 2018). The observation of an increased cell signal down to 100 µm electrodes thus corresponds to this dependency. Nevertheless, there are technical limitations of the impedance analyzer as well as the multiplexer at high impedances. In fact, our multiplexer is optimized for high impedance measurements and therefore allows the analysis of objects with high self-impedances. However, the measureable signal window decreases with smaller electrodes and get clearly limited (Supplementary Fig. S2). This could explain the absence of an additional cell signal increase for the 50 µm electrodes. Furthermore, with higher electrode impedance the background noise also increases. The determined background noise levels were in the range of 0.15% for both materials up to 100 µm electrode (Au) and 200 µm electrode (ITO), respectively. For smaller electrodes the noise increases (50 µm Au 0.25%, 100 µm ITO 0.28%, 50 µm ITO 0.39%). This also demonstrates the increasing technical limitation of the impedance analyzer for electrodes smaller than 100 µm in diameter. Based on the background noise and maximum cell signal, signal-noise-ratios (SNR) were calculated (Fig. 2C). While for Au electrodes SNRs from 850 (200 µm) up to 1360 (IDE) could be achieved (except for 50 µm with a SNR of 528), the ITO electrodes achieved significant lower SNRs (174 for 50 µm, 224 for 100 µm, 141 for 200 µm and 101 for IDE). Especially for the IDE structures this means a drastically decrease by a factor of 13 in comparison to a factor of 6 for 200 µm, 4.6 for 100 µm and 3 for 50 µm electrodes. Taken together the drastic cell signal loss for large size electrodes (up to 90%) as well as the drastic lowered SNR (up to factor 13) are probably the reason why large size electrode arrays made of ITO are not observed for impedimetric based cell assays in the literature.

3.3. Equivalent circuit model based determination of cell parameter

For the FEM based simulation and optimization of ITO multi-electrode arrays to achieve an optimum cell signal, the knowledge of the electrochemical cell parameters is crucial. Thus, we extended the equivalent circuit model (ECM) of the cell-electrode-interface (see Fig. 1D) for the cell layer resistance R_{cell} and C_{cell} capacitance (Fig. 3A). The fitting is performed in a two-step process, where in the first step the impedance magnitude and phase angle spectra of the cell-free electrodes were fitted to determine the electrode-electrolyte dependent parameters CPE_{el} and R_S as well as L_{ITO} (observed inductance) for ITO microelectrodes. In the second step, the determined electrode-

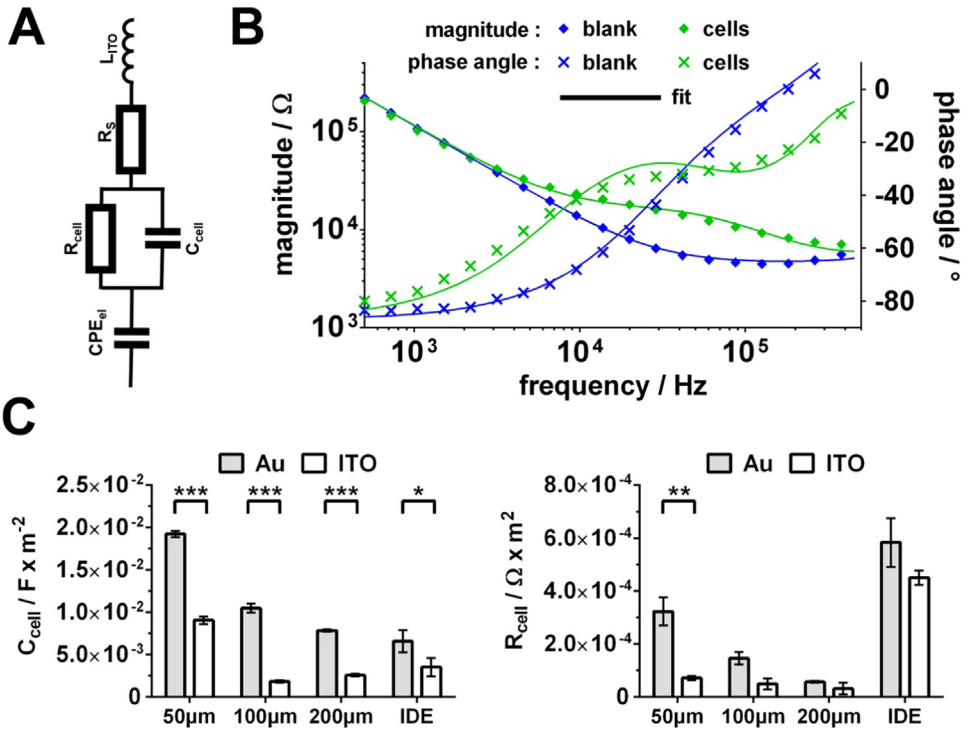

Fig. 3. Equivalent circuit model derived cell layer parameters. (A) Equivalent circuit model for the electrode-cell-interface. (B) Exemplarily results for the two stage fitting process derived impedance magnitude and phase angle spectra. (C) Statistical analysis of the equivalent circuit model derived cell layer capacitance and resistance (n = 3, mean ± sem, * $p < 0.05$, ** $p < 0.01$, *** $p < 0.001$).

electrolyte dependent parameters were fixed and R_{cell} and C_{cell} were determined. The fitting results are exemplarily shown in Fig. 3B. The determined cell layer capacitance for all arrays (n = 3) revealed significant lowered values for ITO electrodes. Furthermore, for Au electrodes the cell layer capacitance decreased with an increased electrode size from 1.9×10^{-2} F/m^2 down to 7×10^{-3} F/m^2. In contrast, ITO electrodes larger than 50 µm revealed an increase of the cell layer capacitance with an increase of electrode size with 2×10^{-3} F/m^2 up to 4×10^{-3} F/m^2. Presuming the cell layer on the different materials are comparable, the determined cell layer capacitance should be comparable. Nevertheless, the individual material characteristics like the surface topology (see Fig. 1B) clearly can lead to differences in the determined values. The analysis of the cell layer resistance again revealed lower values for ITO electrodes (7×10^{-5} Ω × m^2) in comparison to Au electrodes (3×10^{-4} Ω × m^2). Although a significant difference was only observable for the 50 µm electrodes. Interestingly, for both materials the cell layer resistance decreased with increasing electrode size except the IDEs that revealed the highest cell layer resistance (ITO 4.5×10^{-4} Ω × m^2, Au 6×10^{-4} Ω × m^2). Perhaps this is related to the specific layout with its symmetric finger electrodes. Nevertheless, such high cell layer resistance values can only be achieved with an intact confluent layer within the whole well. When the layer is damaged on a small area on the electrodes, the cell signal and therefore the cell layer resistance drastically decreases (Eichler et al., 2015).

3.4. ECM based cell-electrode interface analysis in combination with FEM simulation allows simulation and optimization of transparent ITO multielectrode arrays for sensitive cell monitoring

With the aim of detailed analysis and optimization of multielectrode arrays for cell-based applications using FEM simulations, we created models of the IDE (Fig. 4A) and microelectrode (Supplementary Fig. S3) array (one well) in COMSOL Multiphysics. In a first step, we evaluated the possibility to simulate the electrode-electrolyte-interface based on the ECM derived specific parameters. Since a CPE is hardly possible in the FEM model, we simplified it to a surface impedance with CPE_A values as a capacitance. Based on the determined CPE_n values above 0.92 the CPE represents almost an ideal capacitance. For the material properties, gold was chosen from the reference material library. The conductivity for ITO is described in the literature in the range of 10^4 S/m (Granqvist and Hultåker, 2002; Hosono et al., 2002), which is in line with values of 2×10^4 S/m for our optimized processed ITO layers that we used for the FEM simulation. Thus, we were able to simulate the frequency dependent potential field (Fig. 4A, Supplementary Fig. S3) as well as the current densities (Fig. 4B) for the different layouts. The exemplarily depicted frequencies were selected where the maximum cell signal occurs (IDEs 20 kHz, microelectrodes 100 kHz). While there are obviously drastic differences for the potential and current density of the different layouts, there are also small differences in the current density observable when the materials are compared. Thus, the Au electrodes show a higher current flow, which correlates with a lowered impedance. Next, impedance spectra were calculated based on the FEM simulation for all used electrode array types, which correlated well with the measured spectra (Fig. 4C). Except the observed inductive effect for ITO microelectrodes in the higher frequency range all spectrum characteristics matched. Since this proved our FEM based models, we started with an initial analysis of the geometry influence on the impedance spectra. In detail, we varied the electrode layer thickness for the ITO IDE array, where the loss of cell signal was quite critical (Fig. 4D). The simulation results showed a substantial improvement for the impedance magnitude by increasing the layer thickness to 1400 nm or 2100 nm, while a further thickening resulted in only minor improvements. To verify the validity of our FEM simulation derived results, ITO IDE arrays were produced with a layer thickness of 2100 nm. Again, the FEM simulation derived impedance spectra matched well with the measured data. Additionally, we performed the electrode layer thickness analysis for ITO microelectrode arrays (Supplementary Fig. S4). Except for the inductive effect, all features of the spectra matched and there was an improvement for the impedance observable with an increase of the layer thickness, although the effect was smaller in comparison to the IDE layout. With regard to the initially performed equivalent circuit modelling derived spreading resistance, the FEM simulation reveals that the observed high electrode layer thickness dependency of the electrode impedance, and therefore, the material resistance reflects a certain when not the highest of proportion of R_S at least for ITO IDE arrays (see Fig. 1D).

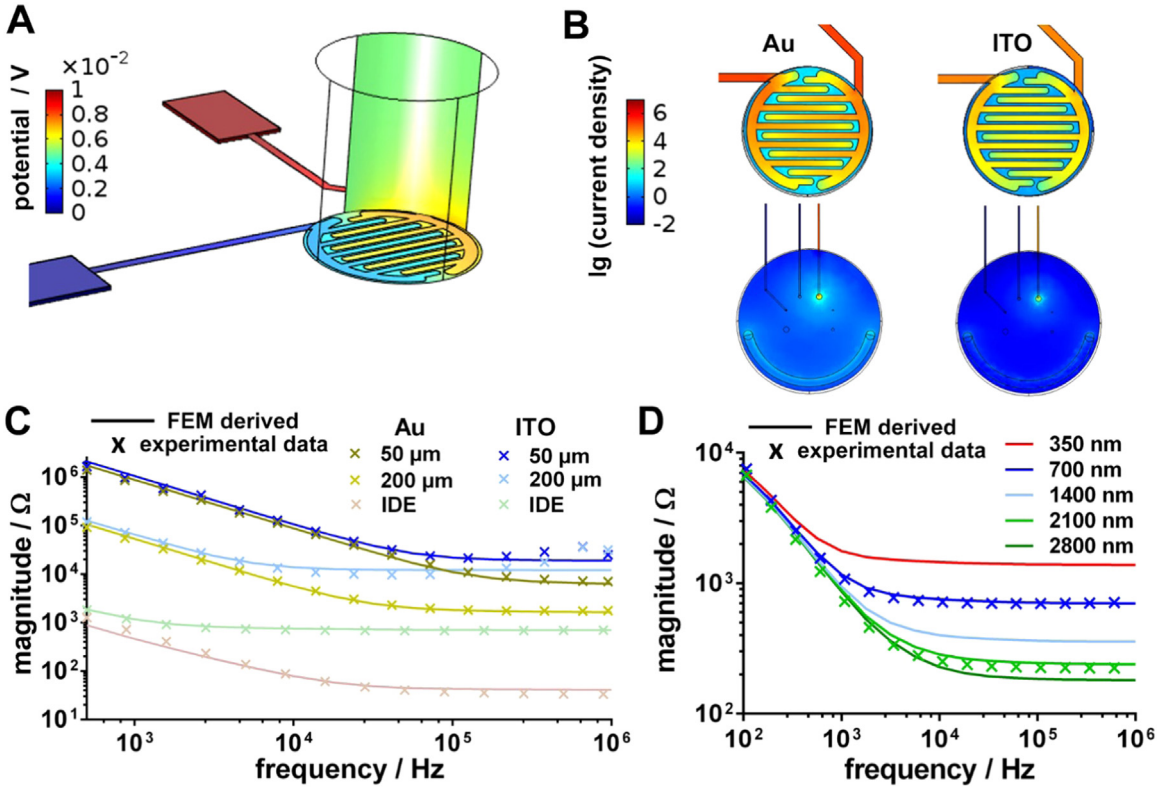

Fig. 4. FEM simulation derived impedance spectra for geometric parameter analysis. (A) FEM model of a single well for the IDE layout with surface potential at 20 kHz. (B) FEM simulation derived current density distribution for the different electrode geometries and materials (IDE 20 kHz, microelectrode layout 100 kHz). (C) Comparison of FEM simulation and experimental derived impedance magnitude spectra for the different electrode array layouts and materials. (D) Comparison of FEM simulation and experimental data derived impedance magnitude spectra for different electrode layer thicknesses (IDE layout made of ITO).

Although the simulation and analysis of the electrode impedance itself offers already a good possibility for optimization of multielectrode array by lowering the overall array impedance, there is still the major question which effort in optimization of the electrode impedance leads to certain optimization of the cell signal. Thus, we wanted to go beyond the solely simulation of the electrode-electrolyte system and include the cell layer into our model for obtaining cell signals from our simulation. For these reason cell layer electrical parameters of the used HEK-A cells were already determined (see Fig. 3). For being able to resolve all small-scale layers and objects and avoid exponential increase of simulation time, we used a simplified 3D model with only a single circular electrode (Fig. 5A) where the electrode diameter is varied as well as the connecting path length and the electrode layer thickness. The latter one is equivalent for the conducting path width, which could also be increased. For the cell layer a cylinder with a height of 5 µm was introduced that cover the culture area. On the surface of this cell layer model a surface capacitance was applied with the averaged values for ITO electrodes larger than 50 µm in diameter (C_{cell} 3×10^{-3} F/m^2, R_{cell} 1.8×10^{-4} Ω × m^2) that were derived from the ECM fitting (see Fig. 3C).

For validation, we started with FEM simulations of 100 µm and 200 µm electrodes with and without cell layer. The obtained impedance magnitude spectra were used to calculate the cell signal (relative impedance spectra), which correlated well with the impedimetric measured spectra (Fig. 5B). For both simulated spectra, a slight spectrum shift to lower frequencies could be observed while maximum cell signal correlated well. An obvious explanation for the slight shift is the use of the averaged electrical cell parameters.

Encouraged by this results we started with a detailed parameter dependency study where the influence of electrode layer thickness, conducting path length and electrode size on the cell signal was analyzed (Supplementary Fig. S5). Moreover, using the maximum cell signals for each simulation derived relative impedance spectrum and the previous determined background noise values, SNRs were calculated (Fig. 5C, Supplementary Fig. S6). This data set reveals that for small ITO electrodes good SNRs can be achieved even for longer conducting path lengths. Moreover, the SNR can be further increased with a thicker electrode layer. But for electrode layer thickness increase beyond 1400 nm the gain in SNR is much smaller. In contrast, to small electrodes large ITO electrodes show a drastic lowered SNR profile. Looking at the 2 mm electrode diameter that comprises an electrode area of 3.14 mm^2 (similar to the IDE) the SNRs are clearly decreased. Since our 5 × 5 cm IDE array comprises conducting path lengths in the range of 5–20 mm it is obvious that although the impedance magnitude can be clearly lowered (See Fig. 4D) only SNRs below 200 for short and below 100 for longer conducting paths can be achieved. An additional increase of electrode layer thickness would only lead to minor improvement and will never reach SNR levels of Au IDE arrays (> 1000) (see Fig. 2C). Furthermore, the increase of the ITO layer thickness beyond 700 nm limits the optical transmission properties, especially in the blue and green wavelength range (Supplementary Fig. S7), which is in line with previous observations (Kim et al., 1999). Additionally, the sputter time drastically increases for such thick layers. Based on the simulation results and the drawn conclusions, we searched for an alternative. Thus, a combined material IDE array with a conventional 700 nm thick ITO layer is the first layer followed by a second 350 nm thick Au layer that covers the contact pads, and conducting paths right up to the finger structures. This layer order has the advantage that no additional adhesion layer is needed for the Au layer. Knowing that the additional structure layer increases fabrication efforts with additional structuring steps as well as additional masks, we wanted to evaluate with our FEM simulation model how much this effort would increase the cell signal as well as the SNR. Thus, we included the Au support layer in our FEM model and simulated the impedance spectra with and

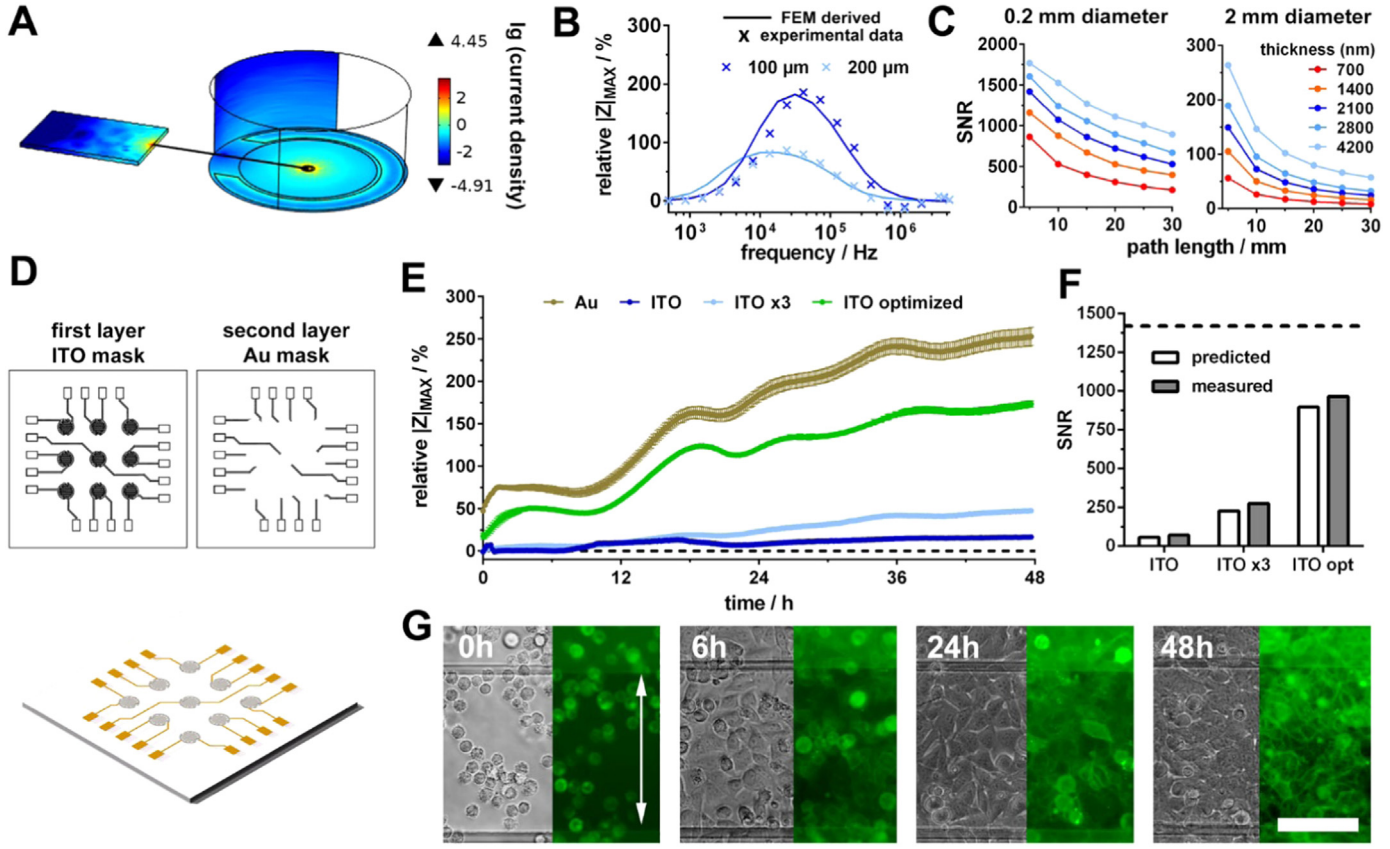

Fig. 5. FEM simulation based optimization of multielectrode array layout for large area electrodes made of ITO. (A) Simplified FEM model with integrated cell layer model for analysis of effect of electrode size and connecting paths geometry on the cell signal. Exemplarily the current density distribution for an ITO electrode with 200 µm diameter at 100 kHz is shown. (B) FEM simulation derived cell signals (relative impedance spectra) for two electrode diameters in comparison to experimental data derived spectra. (C) Analysis of connecting paths length in combination with electrode size (two diameters) on the signal-noise-ratio (SNR) for HEK-A cell layers. (D) Optimized two layer layout of the interdigital electrode array with supporting gold structures extended up to the finger structures. (E) Maximum Cell signal traces over time of HEK-A cells (n = 3, mean ± sem). (F) Comparison of SNRs predicted by FEM simulation and from experiment. Dashed line represents SNR of arrays made of gold. (G) Demonstration of parallel optical monitoring (transmission and fluorescence images from selected time points) of HEK-A cells expressing a GFP-labeled cell membrane marker. White arrow marks the transparent electrode finger (scale bar = 100 µm).

without the cell layer. The derived cell signal (relative impedance spectrum) revealed a clear improvement with a maximum of 160% (Supplementary Fig. S8) and more strikingly, a SNR of 900. Encouraged by this prediction, we designed and ordered the needed mask as well as produced the optimized ITO IDE array with Au support structure. Additionally, we fabricated ITO IDE arrays with a three-fold thicker electrode layer (2100 nm – labeled as ITO x3) for comparison. For the experiment, a modified HEK-A cell line was used that expresses a GFP-labeled cell membrane marker. The cells were seeded on the arrays and optically as well as impedimetrically monitored over time (Fig. 5E, G). While the optical monitoring revealed the suitability for transmission and fluorescence microscopy, the maximum relative impedance traces showed the minor improvement of the increased ITO layer thickness. More strikingly, the optimized ITO IDE layout showed a clear improvement of the cell signal with values after 48 h of 170% maximum relative impedance (cell signal) for “ITO optimized” in comparison to 250% for Au, 17% for ITO and 48% for “ITO x3″. Additionally, the measured relative impedance spectra (cell signal) at 48 h correlates well with the predicted spectrum (Supplementary Fig. S8). The pronounced shift could be due to the differences between the symmetric IDE layout and our simplified FEM model with a circular measurement electrode. Concerning the SNR, our prediction for the ITO arrays matches well with the measurement derived values (Fig. 5F) with 56 vs. 72 for ITO, 228 vs. 275 for “ITO x3″ and 896 vs. 967 for “ITO optimized”. This proves the validity and prediction power of our approach.

4. Conclusion

Taken together, our combined ECM and FEM simulation approach revealed the capability to predict not only electrochemical characteristics of electrode-electrolyte interfaces, but also of cell layers and derived cell signals and SNRs. Based on this, the layout of an ITO IDE multielectrode array could be optimized resulting in a cell signal increase by the factor of ten. Furthermore, this approach could be easily extended to other materials. With increasing array size (Eichler et al., 2015; Solly et al., 2004) loss in cell signal can occur also for high conductive materials like gold, especially when layer thickness is aimed to be reduced because of e.g. costs. Thus, our combined ECM and FEM simulation approach can be a useful method to prevent elaborative fabrication and evaluation cycles as well as experimental trials for numerous designs, which is costly and time-consuming.

Acknowledgment

This work was funded by the Federal Ministry of Education and Research (BMBF, Regional Growth Core BioSAM, Project: NAPYS Grant no. 03WKCL02G). Impedance analyzer and clean room were funded by the Free State of Saxony and the European Union (SMWK/EFRE). The image acquisition facility (AFM) was funded by the Free State of Saxony and the European Union (SMWK/EFRE) (Grant no. 100193539). Furthermore, we want to thank Prof. Bernd Abel from Leibniz-IOM Leipzig for the COMSOL Multiphysics support.

Appendix A. Supplementary material

Supplementary data associated with this article can be found in the online version at doi:10.1016/j.bios.2018.09.095.

References

Canali, C., Heiskanen, A., Muhammad, H.B., Hoyum, P., Pettersen, F.J., Hemmingsen, M., Wolff, A., Dufva, M., Martinsen, O.G., Emneus, J., 2015. Biosens. Bioelectron. 63, 72–79.

Choi, C.K., English, A.E., Jun, S.-I., Kihm, K.D., Rack, P.D., 2007. Biosens. Bioelectron. 22 (11), 2585–2590.

Dean, D.A., Ramanathan, T., Machado, D., Sundararajan, R., 2008. J. Electrostat. 66 (3–4), 165–177.

Eichler, M., Jahnke, H.G., Krinke, D., Muller, A., Schmidt, S., Azendorf, R., Robitzki, A.A., 2015. Biosens. Bioelectron. 67, 582–589.

Frank, R., Klenner, M., Azendorf, R., Bartz, M., Jahnke, H.G., Robitzki, A.A., 2017. Biosens. Bioelectron. 93, 322–329.

Frank, R., Klenner, M., Zitzmann, F.D., Schmidt, S., Ruf, T., Jahnke, H.-G., Denecke, R., Robitzki, A.A., 2018. Electrochim. Acta 259, 449–457.

Fuller, T.F., Harb, J.N., 2018. Electrochemical Engineering. Wiley.

Giaever, I., Keese, C.R., 1984. Proc. Natl. Acad. Sci. USA 81 (12), 3761–3764.

Granqvist, C.G., Hultåker, A., 2002. Thin Solid Films 411 (1), 1–5.

Gross, G.W., Wen, W.Y., Lin, J.W., 1985. J. Neurosci. Methods 15 (3), 243–252.

Hosono, H., Ohta, H., Orita, M., Ueda, K., Hirano, M., 2002. Vacuum 66 (3), 419–425.

Jahnke, H.G., Rothermel, A., Sternberger, I., Mack, T.G., Kurz, R.G., Panke, O., Striggow, F., Robitzki, A.A., 2009. Lab Chip 9 (10), 1422–1428.

Kim, H., Gilmore, C.M., Piqué, A., Horwitz, J.S., Mattoussi, H., Murata, H., Kafafi, Z.H., Chrisey, D.B., 1999. J. Appl. Phys. 86 (11), 6451–6461.

Kisler, K., Kim, B.N., Liu, X., Berberian, K., Fang, Q., Mathai, C.J., Gangopadhyay, S., Gillis, K.D., Lindau, M., 2012. J. Biomater. Nanobiotechnol. 3 (2A), 243–253.

Martin, M.H., Lasia, A., 2011. Electrochim. Acta 56 (23), 8058–8068.

Mittal, N., Rosenthal, A., Voldman, J., 2007. Lab Chip 7 (9), 1146–1153.

Panke, O., Weigel, W., Schmidt, S., Steude, A., Robitzki, A.A., 2011. Biosens. Bioelectron. 26 (5), 2376–2382.

Schmid, Y.R.F., Bürgel, S.C., Misun, P.M., Hierlemann, A., Frey, O., 2016. ACS Sens. 1 (8), 1028–1035.

Solly, K., Wang, X., Xu, X., Strulovici, B., Zheng, W., 2004. Assay. Drug Dev. Technol. 2 (4), 363–372.

Thakur, M., Mergel, K., Weng, A., Frech, S., Gilabert-Oriol, R., Bachran, D., Melzig, M.F., Fuchs, H., 2012. Biosens. Bioelectron. 35 (1), 503–506.

Thomas Jr., C.A., Springer, P.A., Loeb, G.E., Berwald-Netter, Y., Okun, L.M., 1972. Exp. Cell Res. 74 (1), 61–66.

Zareidoost, A., Yousefpour, M., Ghaseme, B., Amanzadeh, A., 2012. J. Mater. Sci. Mater. Med. 23 (6), 1479–1488.

Zitzmann, F.D., Jahnke, H.G., Nitschke, F., Beck-Sickinger, A.G., Abel, B., Belder, D., Robitzki, A.A., 2017. Lab Chip 17 (24), 4294–4302.